A&A 644, L8 (2020)
https://doi.org/10.1051/0004-6361/202039232

Astronomy & Astrophysics

Letter to the Editor

X-rays observations of a super-Chandrasekhar object reveal an ONe and a CO white dwarf merger product embedded in a putative SN Iax remnant⋆

Lidia M. Oskinova[1,2], Vasilii V. Gvaramadze[3,4,5], Götz Gräfener[6], Norbert Langer[6,7], and Helge Todt[1]

[1] Institute of Physics and Astronomy, University of Potsdam, 14476 Potsdam, Germany
e-mail: lida@astro.physik.uni-potsdam.de
[2] Department of Astronomy, Kazan Federal University, Kremlevskaya Str 18, Kazan, Russia
[3] Sternberg Astronomical Institute, Lomonosov Moscow State University, Moscow 119234, Russia
[4] Space Research Institute, Russian Academy of Sciences, Moscow 117997, Russia
[5] Evgeni Kharadze Georgian National Astrophysical Observatory, Abastumani 0301, Georgia
[6] Argelander-Institut für Astronomie, Universität Bonn, Bonn, Germany
[7] Max-Planck-Institut für Radioastronomie, Bonn, Germany

Received 21 August 2020 / Accepted 25 November 2020

ABSTRACT

The merger of two white dwarfs (WDs) is a natural outcome of the evolution of many binary stars. Recently, a WD merger product, IRAS 00500+6713, was identified. IRAS 00500+6713 consists of a central star embedded in a circular nebula. The analysis of the optical spectrum of the central star revealed that it is hot, hydrogen, and helium free, and it drives an extremely fast wind with a record breaking speed. The nebula is visible in infrared and in the [O III] λ5007 Å line images. No nebula spectroscopy was obtained prior to our observations. Here we report the first deep X-ray imaging spectroscopic observations of IRAS 00500+6713. Both the central star and the nebula are detected in X-rays, heralding the WD merger products as a new distinct type of strong X-ray sources. Low-resolution X-ray spectra reveal large neon, magnesium, silicon, and sulfur enrichment of the central star and the nebula. We conclude that IRAS 00500+6713 resulted from a merger of an ONe and a CO WD, which supports earlier suggestion for a super-Chandrasekhar mass of this object. X-ray analysis indicates that the merger was associated with an episode of carbon burning and possibly accompanied by an SN Iax. In X-rays, we observe the point source associated with the merger product while the surrounding diffuse nebula is a supernova remnant. IRAS 00500+6713 will likely terminate its evolution with another peculiar Type I supernova, where the final core collapse to a neutron star might be induced by electron captures.

Key words. white dwarfs – stars: evolution – X-rays: stars – X-rays: individuals: IRAS 00500+6713

1. Introduction

White dwarfs (WDs) are the degenerate remnants of stars born with an initial mass of $M_{\rm init} \lesssim 10\,M_{\odot}$. WDs orbiting each other in a binary system emit gravitational waves leading to the gradual orbit shrinking and the eventual merger. The WD mergers are accompanied by explosive events, and the outcome of the merger depends on the chemical compositions and masses of involved WDs. Likely the most common outcome is a supernova (SN) type Ia which completely disrupts the merger product (Maoz et al. 2014). However, when a WD involved in a merger descends from an intermediate mass star ($M_{\rm init} \approx 8..10\,M_{\odot}$), the merger could eventually lead to the creation of a neutron star (NS, Saio & Nomoto 2004). Schwab et al. (2016) show that a merger of two carbon-oxygen WDs can result in a stable, super-Chandrasekhar mass object. The creation of a super-Chandrasekhar object could also result from a merger of even more massive WDs accompanied by a peculiar SN, for example SN Iax (e.g., Foley et al. 2013; Kashyap et al. 2018). However, while expected to be numerous, neither the remnants of such SNe nor the surviving merger products have been firmly identified.

Recently, Gvaramadze et al. (2019) have claimed that IRAS 00500+6713 is a super-Chandrasekhar mass object. This object consists of a central star embedded in a circular nebula seen in mid-infrared (IR, Fig. 1) and the [O III] narrow band filter (Kronberger et al. 2014). The optical spectrum is dominated by strong and broad oxygen emission lines and in this respect resembles spectra of WO-type stars. The spectral analysis has revealed that the central star is hot, hydrogen, and helium free; consists mainly of carbon and oxygen; and drives a wind with a record breaking speed (Table 1). It is suggested that IRAS 00500+6713 resulted from the merger of two CO WDs, although the possibility that a higher mass ONe WD participated in the merger is reserved. No spectra of the nebula could be obtained and its chemical composition is not known, preventing firm conclusions on the nature of WDs involved in the merger process and the fate of the merger product.

In this Letter, we report on the first deep X-ray observation of IRAS 00500+6713 and the first spectroscopic investigation of

⋆ Based on the observations with the id numbers 0841640101, 0841640201 obtained with the ESA science mission *XMM-Newton*.

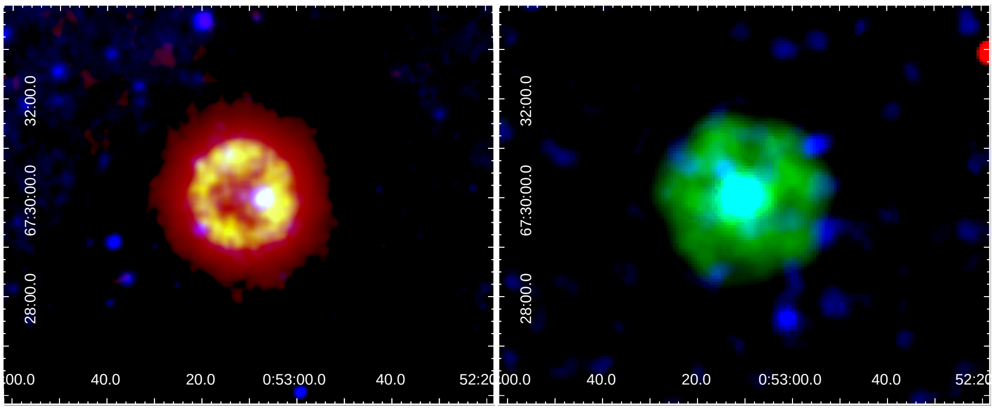

Fig. 1. Images of IRAS 00500+6713 in mid-infrared and X-ray wavelength ranges. *Left panel*: IR Wide-field Infrared Survey Explorer (WISE) image: red and green correspond to 22 μm at two intensity scales, and blue corresponds to 12 μm. A ring-like structure with a diameter of ∼2′ is seen within the nebula. *Right panel*: X-ray EPIC image: red: 0.2–0.7 keV, green: 0.7–1.2 keV, blue: 1.2–7.0 keV. The adaptively smoothed image shows that X-ray emission uniformly fills the whole ∼4′ extent of the IR nebula. At the distance of IRAS 00500+6713, 1′ corresponds to 0.86 pc. The coordinates are in units of RA (J2000) and Dec (J2000) on the horizontal and vertical scales, respectively.

the nebula. In Sect. 2, we describe the new X-ray data. An X-ray spectroscopic analysis of the central star is given in Sect. 3, while the first nebula spectra are analyzed in Sect. 4. Section 5 presents our explanations of the results and the concluding remarks, while a detailed description of the X-ray fitting procedure is presented in the appendix.

2. Observations: The central star and its nebula are luminous X-ray sources

Observations were obtained with the X-Ray Multi-Mirror Mission (*XMM-Newton*) of the European Space Agency (ESA). The three X-ray telescopes of *XMM-Newton* illuminate five different instruments, which always operating simultaneously and independently. The useful data were obtained with the three focal instruments: MOS1, MOS2, and pn, which together form the European Photon Imaging Camera (EPIC). The EPIC instruments have a broad wavelength coverage of 1.2−60 Å and allow low-resolution spectroscopy with ($E/\Delta E \approx 20{-}50$). The log of the *XMM-Newton* observations is given in Table A.1. After rejecting high-background time intervals, the cumulative useful exposure time was ≈18 ks for the EPIC pn and ≈31 ks for the EPIC MOS cameras. The data were analyzed using the *XMM-Newton* data analysis package SAS[1]. Throughout this paper, X-ray fluxes and luminosities are given in the full 0.2–12.0 keV energy band, unless specified otherwise.

The *XMM-Newton* observations have revealed astonishing X-ray properties of IRAS 00500+6713 (Fig. 1 and Table 1). Both the central star and the nebula are clearly detected, heralding the WD merger products as a new distinct type of strong X-ray sources.

3. Analysis of the central star X-ray spectra uncovers carbon and oxygen burning ashes

The central star is more X-ray luminous than single massive OB and Wolf-Rayet (WR) stars (Nebot Gómez-Morán & Oskinova 2018). The optical spectrum of the central star is formed in its powerful wind similarly to the massive H- and He-free WO stars, yet its X-ray luminosity is orders of magnitude higher compared to the latter (Oskinova et al. 2009).

The X-ray spectra (Fig. 2) and the central star light curve (Fig. A.1) were extracted using standard X-ray analysis tools (see Appendix) from a circle with a diameter of 20″. As the background area, we selected an annulus which traces the full extent of the diffuse X-ray emitting nebula around the point source. Hence, the contribution of the nebula emission to the spectrum of the central star should be small. The pile-up is negligible.

The pn light curve binned by 600 s is shown in Fig. A.1. The standard timing analysis procedures were employed to search for a period, but periodicity was not detected.

The EPIC spectra were analyzed using the spectral fitting software *Xspec* (Arnaud et al. 1996). The spectra of collisionally-ionized optically thin plasma were computed with the *apec* model (and its modifications) and the corresponding atomic database *AtomDB* (Smith et al. 2001). The X-ray spectra are dominated by emission lines of Fe, as well as the products of He- and C-burning such as C, N, O, Mg, Ne, Si, and S (Figs. 2 and A.2). The metal abundances measured from the model fitting to the observed low-resolution spectra are shown in Table 1 using the procedure described in Appendix C.

X-ray emitting plasma in the central star has a broad range of temperatures (Tables 1 and A.2) – assuming purely thermal plasma, temperatures up to ∼100 MK are required to reproduce the observed spectra. On the other hand, including a nonthermal spectral component described by a power-law improves the spectral fits. In this case, the maximum thermal plasma temperature is ∼20 MK. Plasma could be heated to such high temperatures by the shocks in the stellar wind of the central star in IRAS 00500+6713, while the nonthermal radiation could be powered by particle acceleration in the expected presence of a magnetic field (Gvaramadze et al. 2019).

The central star in IRAS 00500+6713 has a high mass-loss rate and a CO-rich wind which should effectively absorb X-rays. We searched for the presence of K-shell edges in the X-ray spectrum of the central star, but could not confidently detect them. This rules out an origin of X-ray emission at the base of the wind or implies that the hot and cool wind components are spatially distinct.

The optical spectrum of the central star was analyzed by means of a nonlocal thermodynamic equilibrium stellar atmosphere model, which did not account for X-rays. The carbon and oxygen abundances were derived and resulted in the ratio of

[1] www.cosmos.esa.int/web/xmm-newton/what-is-sas

Table 1. Parameters of the central star and the nebula in IRAS 00500+6713 determined from optical (Gvaramadze et al. 2019) and X-ray (this work) spectroscopy.

Central star parameters from optical spectroscopy	
$E(B-V)$ [mag]	0.84 ± 0.04
T_* [kK]	211^{+40}_{-23}
$\log L_{\rm bol}/L_\odot$	4.6 ± 0.14
$\log (L_{\rm mech}/[{\rm erg\,s^{-1}}])$	≈ 38.4
Mass-loss rate $\dot{M}$ [$M_\odot\,{\rm yr}^{-1}$]	$(3.5 \pm 0.6) \times 10^{-6}$
Wind velocity v_∞ [km s^{-1}]	$16\,000 \pm 1000$
$X_{\rm C}$	0.2 ± 0.1
$X_{\rm O}$	0.8 ± 0.1
$X_{\rm Ne}$	0.01
Central star parameters from X-ray spectroscopy	
$N_{\rm H}$ [cm^{-2}]	$(1.0 \pm 0.2) \times 10^{22}$
$L_{\rm X}$ (0.2–12 keV) [erg s^{-1}]	$(1.2 \pm 0.2) \times 10^{33}$
$\log L_{\rm X}/L_{\rm bol}$	≈ -5
$\log L_{\rm X}/L_{\rm mech}$	≈ -5
$T_{\rm X}$ [MK]	1–100
$X_{\rm C}$	0.15
$X_{\rm O}$	0.61
$X_{\rm Ne}$	0.10 ± 0.03
$X_{\rm Mg}$	0.04 ± 0.02
$X_{\rm Si}$	0.06 ± 0.04
$X_{\rm S}$	0.04
Nebula parameters from X-ray spectroscopy	
$N_{\rm H}$ [cm^{-2}]	$(1.0 \pm 0.2) \times 10^{22}$
$L_{\rm X}$ (0.2–12 keV) [erg s^{-1}]	$(3.0 \pm 0.2) \times 10^{34}$
$T_{\rm X}$ [MK]	1–20
$X_{\rm C}$	0.72
$X_{\rm O}$	0.13 ± 0.06
$X_{\rm Ne}$	0.13 ± 0.04
$X_{\rm Mg}$	0.02 ± 0.01

Notes. The distance 3.1 kpc was adopted. The O, C, and S abundances were fixed during the fitting of the central star spectra, while only the C abundance was fixed when fitting the nebula spectrum (see appendix). The error bars correspond to 1σ.

$({\rm C/C_\odot})/({\rm O/O_\odot}) \approx 0.6$ (by number) (Gvaramadze et al. 2019). The optical spectrum analyses also hinted at strong Ne enrichment, up to 50% by mass, but magnesium, silicon, and sulfur were not included in the models. In X-ray spectra, the carbon lines are located redward of 30 Å, that is in the spectral range which suffers from the absorption of X-rays in the interstellar medium. Consequently, carbon lines are not detected in the central star X-ray spectra. Hence, during the analysis of X-ray spectra, we adopted the carbon abundance as well as the C/O ratio as derived from optical spectroscopy.

The spectral models which reproduce the observed X-ray spectra of the central star well (Table A.2) have similar abundance ratios and require strong enhancement of carbon-burning ashes, as well as of Si and S. The emission features corresponding to the blends of the Si XIII λ6.65 Å and Si XIV λ6.18 Å lines, as well as of the S XV λ5.04 Å and S XVI λ4.73 Å lines are clearly seen in the spectra displayed in Fig. 2. These lines have their peaks at the temperatures between 10 MK and 26 MK, that is to say in the temperature range covered by our two-temperature spectral models. Therefore we believe that the strong Si and S overabundances detected in the X-ray spectra of the central star are real.

4. The lines of carbon-burning ashes are detected in the nebula spectra

Here we present the first spectroscopy of the nebula of IRAS 00500+6713 (Fig. 2). The nebula images and spectra were obtained with the help of the *ESAS* package which also computes the response functions for extended sources (Appendix B). The extent of the circular X-ray nebula is the same as of the IR nebula detected at 22 μm (Fig. 1). Gvaramadze et al. (2019) attribute the nebula emission to the forbidden lines of [O IV] λ 25.89 μm and [Ne V] $\lambda\lambda$ 14.32, 24.32 μm. We suggest that the warm dust also contributes to the nebula IR emission. The warm dust co-existing with the hot plasma is often observed in the supernova remnants (SNR) (Zhou et al. 2020). The X-ray nebula is brightest in the medium X-ray band (0.7–1.2 keV). A number of faint X-ray point sources are superimposed on the nebula, for now we consider these sources to be unrelated.

The X-ray luminosity of the nebula is in the upper range observed from hot bubbles around massive WR stars (Toalá et al. 2017), and it is significantly higher than the luminosity of diffuse gas in planetary nebulae (Chu et al. 2001; Kastner et al. 2001). Furthermore, the plasma temperature significantly exceeds the temperatures in WR bubbles or planetary nebulae. X-ray emission of these objects is powered by strong shocks which occur when the fast wind driven by the hot central stars rams into material of a slow wind ejected at a previous stellar evolutionary stage. Hydrodynamic simulations of hot WR bubbles and planetary nebulae indicate that mixing processes effectively reduce possible differences in chemical composition of the cool and the hot gas components (Volk & Kwok 1985; Kwok 2000; Toalá & Arthur 2011).

The IRAS 00500+6713 nebula spectrum is dominated by two strong emission features corresponding to the blends of the Mg XI λ9.1 Å and Mg XII λ8.4 Å lines as well as the Ne IX λ13.4 Å and Ne X λ12.1Å lines (Figs. 2, A.3). The blend of the S XVI λ4.7 Å and S XV λ5 Å lines is dramatically weaker in the nebula spectrum compared to the spectrum of the central star. The emission measure of the hot plasma in the nebula is $\sim 10^{55}$ cm^{-3}. Under the crude assumption of a uniform and constant density and that the nebula is solely composed of C, O, Ne, and Mg, the total mass of hot gas is $\sim 0.1\,M_\odot$ (see Appendix C).

5. IRAS 00500+6713: A post WD merger product embedded in a putative SN Iax remnant and evolving toward an electron capture SN

X-ray spectroscopy allowed us to refine the central star abundances and to determine the chemical composition of nebula for the first time (Table 1). These findings call for a reassessment of the nature of IRAS 00500+6713, which we consider below.

5.1. Abundance constrains from X-ray spectroscopy

The central star abundances, in particular the predominance of Si and S, imply a composition resulting from incomplete C and O burning. Indeed, assuming that no major element remained undetected, Si and S make up ~10% of the surface composition whereas Ne and Mg constitute up to ~14%.

In the nebula, Ne and Mg also constitute up to ~15%, whereas the S lines are much weaker in the nebula spectrum compared to the central star spectrum (Fig. 2). Furthermore, the C/O and Ne/O ratios appear to be different in the central star and

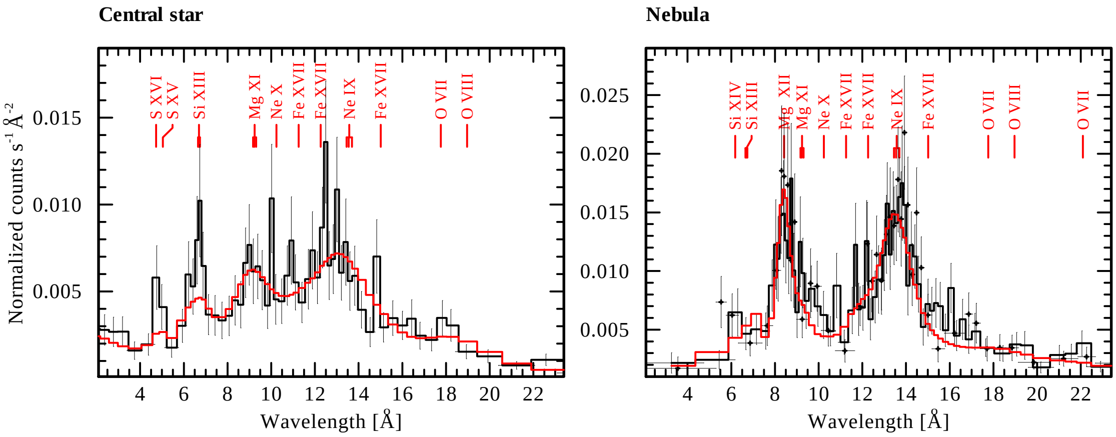

Fig. 2. Low resolution observed (source plus background) EPIC pn X-ray spectra of the central star (*left panel*) and the nebula (*right panel*) in IRAS 00500+6713. The error bars correspond to 3σ. Red histograms show the best-fitting spectral models (see Appendix A and B for details on spectral modeling and the treatment of the background). The prominent emission spectral features are identified at the wavelengths corresponding to the positions of strong emission lines predicted by the *apec* models for plasma with a chemical composition and temperatures similar to that of IRAS 00500+6713.

the nebula: in the latter, $X_{\rm C}/X_{\rm O}, X_{\rm Ne}/X_{\rm O} < 1$, while in the former $X_{\rm C}/X_{\rm O} \gtrsim 1$ and $X_{\rm Ne}/X_{\rm O} \sim 1$.

It is important to keep in mind that the wavelength range of X-ray spectra we study does not include C lines. For the central star, C and O abundances were adopted from Gvaramadze et al. (2019). The later work was based on the analyses of optical spectra and did not account for X-ray emission (not known at that time). For the nebula, we calculated a series of spectral models adopting a different C abundance (two such models are shown in Table B.1), each of them resulting in $X_{\rm C}/X_{\rm O} \gg 1$. However, nebula spectra could also be fitted with the C and O ratio fixed to be the same as in the central star.

5.2. Comments on the central star mass, and comparison of the central star with partially burned accretors and donors of thermonuclear SNe

The surface gravity ($\log g$) of the central star cannot be measured because no photospheric lines are seen in its optical spectrum. Instead, the IRAS 00500+6713 mass estimate relies on its position on the Hertzsprung–Russell diagram (HRD) and the comparison with the evolutionary tracks.

Gvaramadze et al. (2019) determined the luminosity of IRAS 00500+6713, $\log L_{\rm bol}/L_{\odot} \approx 4.6$, from spectral modeling and the *Gaia* distance. Given the H- and He-free composition, and using the WD merger model from Schwab et al. (2016), they conclude that IRAS 00500+6713 is a super-Chandrasekhar object with a mass $\gtrsim$1.5 $M_{\odot}$. We adopted this mass estimate.

Taking the updated abundances into account, we suggest that IRAS 00500+6713 was formed by a merger of a ONe WD and a CO WD with masses $>$1 $M_{\odot}$ and $>$0.5 $M_{\odot}$ correspondingly. Hence our results corroborate the conclusion on the super-Chandrasekhar mass of IRAS 00500+6713. The recent evolutionary calculations of WDs with masses up to 1.307 $M_{\odot}$ show that the luminosity of a WD with the ONeMg core $M_{\rm ONeMg}$ = 1.22 $M_{\odot}$ could approach $\log L_{\rm bol}/L_{\odot} \approx 4.5$; however, these massive WDs posses H-rich envelopes as well as He, while IRAS 00500+6713 is H- and He-free (Lauffer et al. 2018).

It is also informative to compare IRAS 00500+6713 with other sub-Chandrasekhar mass WDs which are H- and He-free and are rich in the ashes of C-, O-, and Si-burning (Shen et al. 2018; Gänsicke et al. 2020, and ref. therein). These runaway WDs (often called LP 40-365-like and D^6-type) belong to a heterogeneous group of objects consisting of partially burned accretors and puffed-up donors of thermonuclear SNe. The central star in IRAS 00500+6713 does not resemble these objects. Without correction for reddening, IRAS 00500+6713 has $M_{\rm G} \approx 2.76$ mag from the *Gaia* DR2 data. This is significantly smaller than the $M_{\rm G}$ of the runaway D^6-type WDs discussed by Shen et al. (2018). Furthermore, the optical spectra of IRAS 00500+6713 and the D^6 & LP 40-365-like WDs are very different – while the later show photospheric spectra and no trace of winds, the former spectrum is formed in a strong outflow. One may speculate that if IRAS 00500+6713 would not collapse in the course of its evolution but instead cool, then it could become a WD with an extreme surface composition; an interesting question is whether such an object would resemble the LP 40-365-like and D^6-type SNe survivors.

5.3. IRAS 00500+6713 stellar wind, remarks on its possible magnetic field, and ruling out a recent SN

The strong stellar wind in IRAS 00500+6713 corroborates the super-Chandrasekhar nature of its central star because objects close to their Eddington limit are expected to launch powerful winds (Gräfener & Vink 2013; Sander et al. 2020). Furthermore, wind acceleration could be aided by a magnetic field as expected in WD mergers (e.g., Beloborodov 2014). It should be noted that while mergers may produce magnetic WDs, there is no strong evidence that they always do so. Conversely, there are strongly magnetic WDs in binaries (Pala et al. 2020).

Whether IRAS 00500+6713 is indeed magnetic is not known. However, Gvaramadze et al. (2019) invoke the theory of rotating magnetic winds (Poe et al. 1989) to qualitatively explain the velocity of the wind in IRAS 00500+6713, while Kashiyama et al. (2019) used a magneto-hydrodynamic model and demonstrate that the optically thick outflow could be launched from the C-burning shell on an ONe core and accelerated by the rotating magnetic field.

The mechanism of the central star X-ray emission is not clear but the very high wind velocity provides an ample energy reservoir for plasma heating. The detection of a nonthermal component in the X-ray spectrum hints that magnetism may also play a role. However, X-rays originating deep in stellar wind would hamper wind acceleration and they would be strongly absorbed – this is not observed, however. Therefore, we tentatively suggest that X-rays are produced in the outer wind regions.

The wind speed, 16 000 km s^{-1}, is comparable to expansion velocities of SN ejecta. This begs the question of whether what we interpret as wind is in fact SNR material coasting at that velocity. To investigate this question, we searched historical astronomical data. Photographic plate observations that were obtained in the *Hamburger Sternwarte* and digitized by the *APPLAUSE* project[2] show that IRAS 00500+6713 had $V \approx$ 15 mag in November 1926, which is similar to its present day $V = 15.44$ mag (The Guide Star Catalog 2.3, 2006) or $V = 15.23$ mag (The NOMAD-1 Catalog, 2005). The photometric monitoring of IRAS 00500+6713 in 2017–2019 shows only small variability around $V = 15.49$ mag, not exceeding 0.05 mag (A. S. Moskvitin, priv. comm.). Thus, the brightness in V remained stable within 0.5 mag during 100 yr. Moreover, the optical spectra have not shown any evolution during the last three years (2017–2020, Gvaramadze et al. 2019; Garnavich et al. 2020). Hence the central star is a stable object and its strong stellar wind is not a sporadic ejecta.

5.4. The high carbon abundance in IRAS 00500+6713 argues against its nature as an electron capture SN

Among a small group of known H- and He-free objects are the stellar remnants of electron-capture SNe (ECSNe). Jones et al. (2019) studied O-Ne deflagrations in WDs as an underlying mechanism of ECSNe. Their 3D hydrodynamic models and the post-processing predicting the ejecta composition imply that ECSNe, which include accretion-induced collapse (AIC) of ONe WDs, could be partial thermonuclear explosions leaving behind a bound ONeFe WD. However, this model predicts a very low C abundance (see e.g., their Table 7). If future analyses of IRAS 00500+6713, UV spectra will reveal a significantly lower C abundance than $X_{\rm C} = 0.2 \pm 0.1$ derived by Gvaramadze et al. (2019), and if it would be shown that ONeFe WDs could have luminosities as high as IRAS 00500+6713, then a bound remnant of an ECSN and its SNR could become an interesting possibility to explain IRAS 00500+6713. However, based on the current data and models, this channel appears unlikely.

5.5. SNe type Iax in a single-degenerate scenario

SNe Iax are a subset of peculiar SNe Ia, which have low luminosities as well as low ejecta velocities and masses (Foley et al. 2013). In their review of SN Iax, Jha et al. (2017) conclude that the results from a CO or a hybrid CONe WD accretes from a He-star companion, approaches the Chandrasekhar mass, and explodes as a deflagration that may leave a bound remnant. Fink et al. (2014) carried out a study of a CO WD explosion in a single-degenerate scenario. The major result of their 3D hydrodynamic models is the occurrence of a bound remnant, which is mostly comprised of the unburnt matter and the ejection of the hot deflagration ashes at velocities up to 14 000 km s^{-1}. Unburnt CO material and ^{56}Ni can be found at all ejecta velocities. Furthermore, the model predicts that the outer layers of the bound remnants are enriched with the iron group and intermediate mass (Si, S) elements. In the ejecta, the abundances of Ne and Mg are significantly lower than O, while O/C ∼ 1.

Leung & Nomoto (2020) carried out 2D simulations of the propagation of deflagration, which leaves a small WD remnant behind and ejects nucleosynthesis materials. The nucleosynthesis and explosion energy depend on the central densities and compositions of the WDs as well as on the flame prescriptions. The model predicts a low mass WD remnant similar to LP 40-365-like and related objects. Furthermore, Leung & Nomoto (2020) considered massive ONeMg WDs resulting from a super-AGB star evolution when the core or shell O-burning is ignited by electron capture and can trigger oxygen deflagration. In these models, ejecta have $X_{\rm Ne}/X_{\rm O} \lesssim 1$ which is similar to the $X_{\rm Ne}/X_{\rm O} \sim 1$ ratio empirically measured in the IRAS 00500+6713 nebula.

Nevertheless, an SN Iax in a single degenerate scenario does not seem to be a likely explanation for IRAS 00500+6713. Firstly, a He-star donor is not observed; secondly, IRAS 00500+6713 did not experience an SN in the last 100 yr; thirdly, the central star is not a low mass WD.

5.6. IRAS 00500+6713 as a result of a ONe and CO WD merger accompanied by an SN Iax and evolving toward an ECSN

In agreement with the suggestion of Gvaramadze et al. (2019), we favor a double-degenerate channel. The hydrodynamic models of a merging ONe ($1.2\,M_\odot$) and CO ($0.6\,M_\odot$) WD binary (Lorén-Aguilar et al. 2009) show a mild nuclear processing of material from the CO dwarf, with some Ne and Mg production. However, this is not compatible with the high Si and S abundances in IRAS 00500+6713. On the other hand, the model remnant WD mass of $1.5\,M_\odot$ fits well to the mass of IRAS 00500+6713 as estimated from its current luminosity.

The higher mass ONe+CO WD merger models (Kashyap et al. 2018) predict that the less massive but larger CO WD is tidally disrupted and forms a hot, low-density accretion disk around the ONe WD. The ignition and explosive disruption of this disk produces a low-energy (∼10^{49} erg) SN, putatively of Type Iax, which leaves the ONe WD largely intact. In these models, the remaining WD re-accretes part of the explosive ejecta, which are highly enriched in Si and S (their Figs. 5 and 6), together with Ne, Mg, and unprocessed C and O. The final mass of the star left behind in this model is ∼$2.2\,M_\odot$ and the predicted $X_{\rm Ne}/X_{\rm O} \approx 0.04$ (see their Table 1), that is to say lower than what we find from X-ray spectroscopy.

In the ONe and CO WD merger accompanied by an SN Iax scenario, the IRAS 00500+6713 nebula is an SNR. Scaling relations based on the Sedov solution (Borkowski et al. 2001; Oskinova 2005) yield the SNR age of ∼1000 yr. SNe Iax can be as dim as $M_{\rm V} = -14$ mag. The SN would then only appear as bright as Sirius ($V = -1.5$ mag); and with a duration of just 2 weeks, it could have been easily missed in the last millennium.

The inner ring-like shell seen in the IR image (Fig. 1, left panel) with the radius $R_{\rm sh} \approx 1$ pc could have been created by the current fast wind of the central star. The distance at which the wind ram pressure is balanced by the thermal pressure in the SNR corresponds to $R_0 = \sqrt{\dot{M}v_\infty/4\pi P_{\rm th}}$, where $P_{\rm th} = (\gamma - 1)E_{\rm th}/V$, $\gamma = 5/3$, $E_{\rm th}$ is the thermal energy of the SN blast wave, $V = (4\pi/3)R^3_{\rm SNR}$, and $R_{\rm SNR}$ is the radius of the nebula. In the Sedov phase, about 72% of the kinetic energy produced by the

[2] https://www.plate-archive.org/objects/dr.3/plates/101_1702
https://www.plate-archive.org/objects/dr.3/plates/101_1696

SN explosion, E_0, is converted into E_{th}. Adopting $E_0 = 2.2 \times 10^{49}$ erg (as in Kashyap et al. 2018), $E_{th} = 1.6 \times 10^{49}$ erg. Using $\dot{M}$ and v_∞ from Table 1, and $R_{SNR} = 1.6$ pc, one finds that $P_{th} = 2 \times 10^{-8}$ dyne cm^2 and $R_0 = 0.4$ pc. This is four times smaller than the observed R_{sh}. This could be explained if E_0 was smaller or if P_{th} was not a constant value but it grew with the radius. For $E_0 = 2.2 \times 10^{49}$ erg and $n_{ISM} = 1\,cm^{-3}$, the age of the SNR is only $t_{SNR} \approx 350$ yr, while for a factor of ten lower value of E_0, the SNR age is $t_{SNR} \approx 1100$ yr. These should be the characteristic times for the merger product to contract to its current size and to develop its very fast wind.

Wang & Liu (2020) provide estimates of the Galactic rates of ONe+CO WD mergers. According to their predictions, there should be 10^6–10^7 ONe+CO WD binaries in the galaxy. Interestingly, such WD binaries belong to a relatively young stellar population (50–100 Myr old), which is in agreement with the host populations of SNe Iax (Jha et al. 2017).

Clearly, more WD merger models are needed to pin down the progenitor masses of the two WDs, which produced IRAS 00500+6713, and to explain its abundance measurements. While current models of WD mergers do not include stellar winds, the discovery of an extreme WO-type wind from the central star in IRAS 00500+6713 demonstrates the urgent need to do so, at least in models of post WD-merger evolution.

The farther evolution of IRAS 00500+6713 is spectacular. Based on its empirical mass loss rate and the expected short remaining lifetime of several 1000 yr, the mass of IRAS 00500+6713 will likely remain above the Chandrasekhar limit. Its fate will therefore be to undergo core collapse and to form a neutron star. Over the course of this event, IRAS 00500+6713 will manage to produce its second SN, possibly in the form of a fast blue optical transient (Dessart et al. 2006; Lyutikov & Toonen 2019).

Acknowledgements. The authors are grateful for the very useful and insightful referee report which allowed to significantly improve the paper. We thank J.M. Drudis for bringing to our attention the paper by Kronberger et al. (2014). L.M.O. acknowledges financial support by the Deutsches Zentrum für Luft und Raumfahrt (DLR) grant FKZ 50 OR 1809, and partial support by the Russian Government Program of Competitive Growth of Kazan Federal University. V.V.G. acknowledges support from the Russian Science Foundation under grant 19-12-00383. G.G. thanks the Deutsch Forschungsgemeinschaft for financial support under Grant No. GR 1717/5-1. Funding for APPLAUSE has been provided by DFG, AIP, Dr. Remeis Sternwarte Bamberg, the Hamburger Sternwarte and Tartu Observatory. Plate material also has been made available from Thüringer Landessternwarte Tautenburg.

References

Arnaud, K. A. 1996, in Astronomical Data Analysis Software and Systems V, eds. G. H. Jacoby, & J. Barnes, ASP Conf. Ser., 101, 17

Asplund, M., Grevesse, N., Sauval, A. J., & Scott, P. 2009, ARA&A, 47, 481

Beloborodov, A. M. 2014, MNRAS, 438, 169

Bohlin, R. C., Savage, B. D., & Drake, J. F. 1978, ApJ, 224, 132

Borkowski, K. J., Lyerly, W. J., & Reynolds, S. P. 2001, ApJ, 548, 820

Chu, Y.-H., Guerrero, M. A., Gruendl, R. A., Williams, R. M., & Kaler, J. B. 2001, ApJ, 553, L69

Dessart, L., Burrows, A., Ott, C. D., et al. 2006, ApJ, 644, 1063

Fink, M., Kromer, M., Seitenzahl, I. R., et al. 2014, MNRAS, 438, 1762

Foley, R. J., Challis, P. J., Chornock, R., et al. 2013, ApJ, 767, 57

Gänsicke, B. T., Koester, D., Raddi, R., Toloza, O., & Kepler, S. O. 2020, MNRAS, 496, 4079

Garnavich, P., Littlefield, C., Pogge, R., & Wood, C. 2020, Res. Notes AAS, 4, 167

Gräfener, G., & Vink, J. S. 2013, A&A, 560, A6

Gvaramadze, V. V., Gräfener, G., Langer, N., et al. 2019, Nature, 569, 684

Jha, S. W. 2017, in Type Iax Supernovae, eds. A. W. Alsabti, & P. Murdin, 375

Jones, S., Röpke, F. K., Fryer, C., et al. 2019, A&A, 622, A74

Kashiyama, K., Fujisawa, K., & Shigeyama, T. 2019, ApJ, 887, 39

Kashyap, R., Haque, T., Lorén-Aguilar, P., García-Berro, E., & Fisher, R. 2018, ApJ, 869, 140

Kastner, J. H., Vrtilek, S. D., & Soker, N. 2001, ApJ, 550, L189

Kronberger, M., Jacoby, G. H., Acker, A., et al., 2014, Asymmetrical Planetary Nebulae VI Conference, 48

Kwok, S. 2000, The Origin and Evolution of Planetary Nebulae

Lauffer, G. R., Romero, A. D., & Kepler, S. O. 2018, MNRAS, 480, 1547

Leung, S.-C., & Nomoto, K. 2020, ApJ, 900, 54

Lorén-Aguilar, P., Isern, J., & García-Berro, E. 2009, A&A, 500, 1193

Lyutikov, M., & Toonen, S. 2019, MNRAS, 487, 5618

Maoz, D., Mannucci, F., & Nelemans, G. 2014, ARA&A, 52, 107

Nebot Gómez-Morán, A., & Oskinova, L. M. 2018, A&A, 620, A89

Oskinova, L. M. 2005, MNRAS, 361, 679

Oskinova, L. M., Hamann, W. R., Feldmeier, A., Ignace, R., & Chu, Y. H. 2009, ApJ, 693, L44

Pala, A. F., Gänsicke, B. T., Breedt, E., et al. 2020, MNRAS, 494, 3799

Poe, C. H., Friend, D. B., & Cassinelli, J. P. 1989, ApJ, 337, 888

Saio, H., & Nomoto, K. 2004, ApJ, 615, 444

Sander, A. A. C., Vink, J. S., & Hamann, W. R. 2020, MNRAS, 491, 4406

Schwab, J., Quataert, E., & Kasen, D. 2016, MNRAS, 463, 3461

Shen, K. J., Boubert, D., Gänsicke, B. T., et al. 2018, ApJ, 865, 15

Smith, R. K., Brickhouse, N. S., Liedahl, D. A., & Raymond, J. C. 2001, ApJ, 556, L91

Snowden, S. L., Collier, M. R., & Kuntz, K. D. 2004, ApJ, 610, 1182

Snowden, S. L., Mushotzky, R. F., Kuntz, K. D., & Davis, D. S. 2008, A&A, 478, 615

Toalá, J. A., & Arthur, S. J. 2011, ApJ, 737, 100

Toalá, J. A., Marston, A. P., Guerrero, M. A., Chu, Y. H., & Gruendl, R. A. 2017, ApJ, 846, 76

Volk, K., & Kwok, S. 1985, A&A, 153, 79

Wang, B., & Liu, D. 2020, Res. Astron. Astrophys., 20, 135

Wilms, J., Allen, A., & McCray, R. 2000, ApJ, 542, 914

Zhou, P., Leung, S. C., Li, Z., et al. 2020, ApJ, accepted [arXiv:2006.15049]

Appendix A: X-ray properties of the central star

Table A.1. Log of the *XMM-Newton* observations of IRAS 00500+6713.

ObsID	Start-date	Exp. time [ks]
0841640101	2019-07-08	19.7
0841640201	2019-07-24	16.8

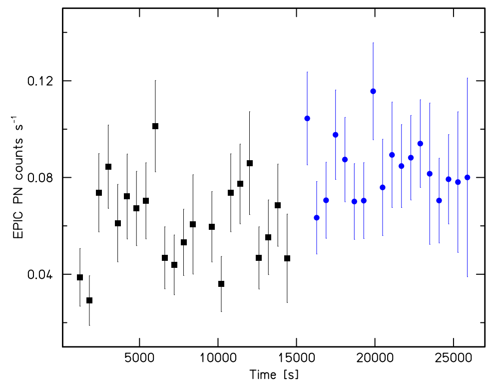

Fig. A.1. *XMM-Newton* EPIC pn light curve of the central star in IRAS 00500+6713. The light-curve was background corrected and binned by 600 s; the error bars correspond to 3σ. The Y-axis is the time after the start of the observation. Black and blue data points refer to the first and second observation, respectively (see Table A.1). For the second observation, the X-axis is shifted by 15 000 s for clarity.

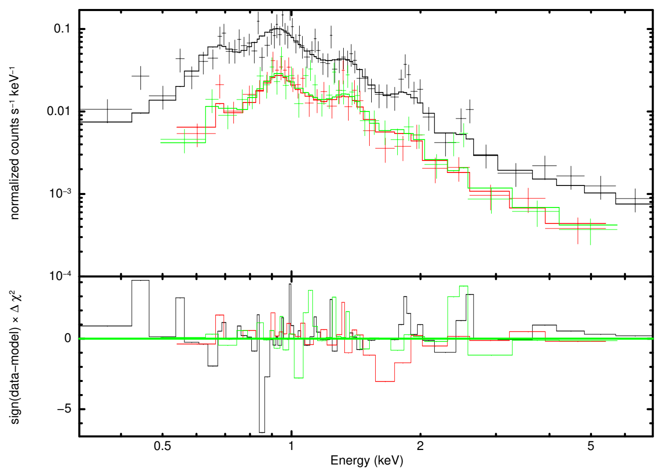

Fig. A.2. Low-resolution X-ray spectra of the central star in IRAS 00500+6713. The EPIC pn (black data points), MOS1 (red data points), and MOS2 (green data points) spectra that were merged over the full exposure time are displayed. The black, red, and green histograms show the best fitting model of a two-temperature plasma and a nonthermal component as well as the residuals as signed contributions.

X-ray spectra of the central star were extracted from a circle with $r = 10''$ centered on the coordinates of IRAS 00500+6713. As the background area, we selected the annulus around the point source which traces the full extent of the X-ray nebula with the outer radius of 40″. Hence, the contribution of nebula emission to the spectrum of the central star should be small or negligible. The event lists were filtered to exclude the intervals of flaring particle background exceeding $0.4\,\mathrm{s}^{-1}$ for pn, and $0.35\,\mathrm{s}^{-1}$ for the MOS cameras. The SAS task *evselect* was used to extract the spectra in the 0.2–10.0 keV range and the binning factor (via the parameter *spectralbinsize*) was set to five. The spectra obtained during each of the two observations (Table A.1) were combined using the *epicspeccombine* SAS task. The three resulting spectra are shown in Fig. A.2 and they were fitted using *apec*, where the element abundances were normalized to solar values relative to hydrogen. Having this caveat in mind, the metal abundances measured from the model fitting to the observed low-resolution spectra shown in Tables A.2 and B.1 are relative to the solar values of Asplund et al. (2009).

Statistically acceptable fits to the observed spectra of the central star were obtained with the absorbed (by using the *tbabs* model, Wilms et al. 2000) multi-temperature *bvtapec*[3] spectral model. The stellar wind of IRAS 00500+6713 is exceptionally fast, with $v_\infty = 16\,000\,\mathrm{km\,s}^{-1}$. If the hot plasma is expanding with a similar velocity, then emission lines observed in the X-ray spectrum are broad. The spectral resolution of EPIC cameras ($\Delta E = 20 - 50$) is not sufficient to resolve even such broad lines. Nevertheless, we found that accounting for line broadening (by setting the velocity parameter to $16\,000\,\mathrm{km\,s}^{-1}$) improves the fitting statistics – for 124 d.o.f., the reduced $\chi^2 = 0.91$ without including the line broadening, while it drops to $\chi^2 = 0.89$ when the line broadening is accounted for.

To determine the abundances, we first tested a model where the interstellar absorbing column density, N_H, and the C, O,

Table A.2. X-ray spectral properties of the central star in IRAS 00500+6713 from fitting its low-resolution EPIC spectra.

Model parameter	Fit value	
spectral model	*2Tbvtapec*	*2Tbvtapec+power*
N_H [10^{22} cm^{-2}]	1.0 ± 0.2	1.0 ± 0.2
kT_1 [keV]	0.27 ± 0.04	0.27 ± 0.04
EM_1 [10^{53} cm^{-3}]	2 ± 1	2 ± 1
kT_2 [keV]	6 ± 2	1.6 ± 1.1
EM_2 [10^{53} cm^{-3}]	0.8 ± 0.1	0.2 ± 0.1
C	600	600
O	1000	1000
Ne	800 ± 200	750 ± 200
Mg	600 ± 300	600 ± 250
Si	1000 ± 900	800 ± 520
S	1000	1000
α		0.9
K (ph keV^{-1} cm^{-2} s^{-1})		$(4 \pm 1) \times 10^{-6}$
Reduced χ^2 for 124 d.o.f.	0.93	0.89
Model F_X [erg cm^{-2} s^{-1}]	$(1.7 \pm 0.2) \times 10^{-13}$	
Luminosity L_X [erg s^{-1}]	$(1.2 \pm 0.2) \times 10^{33}$	
log $L_\mathrm{X}/L_\mathrm{bol}$	−5	

Notes. The ion and the continuum temperatures were assumed to be equal. The line broadening was set to $v = 16\,000\,\mathrm{km\,s}^{-1}$. The abundances shown without errors were not fit but frozen during the fitting process. The abundances which are not shown in the table are at their solar values, expect He and N abundances which are vanishingly small. Observed flux and de-reddened luminosity are in 0.2–12.0 keV band assuming $d = 3.1$ kpc.

[3] A velocity- and thermally-broadened emission spectrum from collisionally-ionized diffuse gas calculated from the AtomDB atomic database, where we assumed identical "continuum" and "line" temperatures.

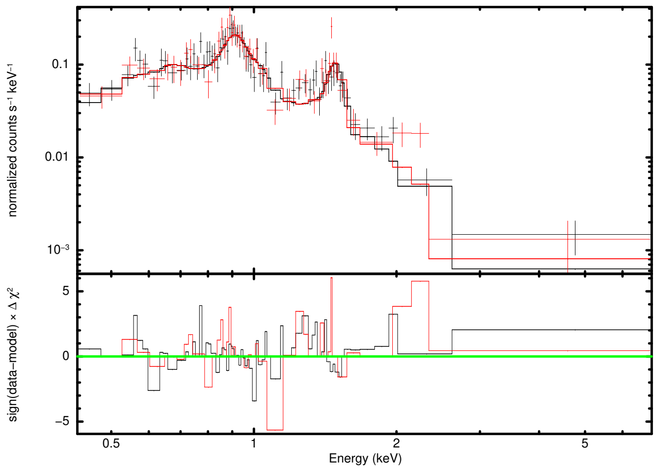

Fig. A.3. Low-resolution X-ray spectra of the nebula in IRAS 00500+6713. The EPIC pn (black and red data points) spectra obtained during two pointings are displayed. The histograms show the best-fitting model (second column in Table A.2) of a two-temperature plasma and the residuals as signed contributions.

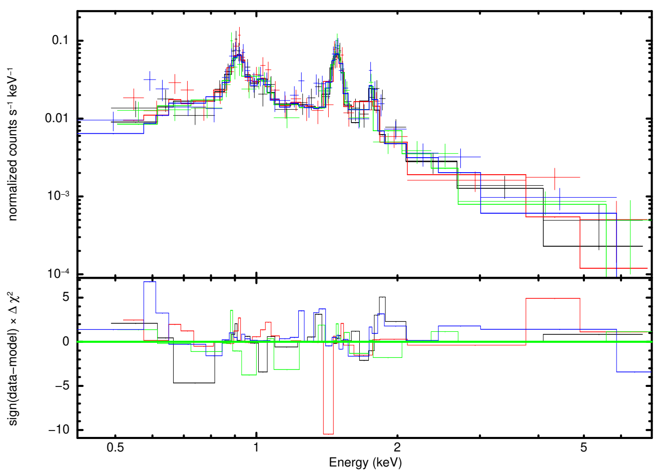

Fig. A.4. Same as in Fig. A.3, but for EPIC MOS1 and MOS2 spectra obtained during two pointings. The histograms show the best-fitting model (fourth column in Table A.2 of a two-temperature plasma), and the residuals as signed contributions.

N, and Mg abundances were considered as free parameters; however, no meaningful constraints on these parameters could be derived. The reddening to the star, $E(B-V)$, is known from the optical (Table 1). Hence, we tested a model with the fixed $N_{\rm H} = 5.8\times10^{21} E(B-V)$ (Bohlin et al. 1978); however, the metal abundances still could not be constrained. The C V λ41 Å and C VI Lyα λ33 Å lines are located in the part of the *XMM-Newton* spectrum which has a low signal-to-noise ratio and which suffers from absorption. Hence, X-ray spectral models are not sensitive to carbon abundances. Therefore, we decided to reduce the parameter space by using the abundance measurements from optical spectroscopy with the carbon and oxygen abundances determined as $C/C_\odot \approx 930$ and $O/O_\odot \approx 1500$ (by number, Gvaramadze et al. 2019). Unfortunately, in *Xspec*, the maximum value of an element abundance cannot exceed 1000. Therefore, we froze the O abundance to 1000 and set the C abundance to 600 to preserve the C/O ratio derived from the optical spectra.

A two temperature model with Ne, Mg, Si, and S abundances being fitting parameters tied among both temperature components produces an excellent quality fit, indicating that an S abundance is very high but very poorly constrained. The strong S line blend at $\lambda\lambda$4.7, 5.0 Å is clearly seen by the naked eye. To roughly match the line strengths, we froze the S abundance to the maximum possible value $S/S_\odot = 1000$. This immediately improved the fitting statistics. The S XVI Lyα line has the maximum emissivity at the temperature 25 MK. This temperature regime is covered by the hottest plasma component in our models, hence we believe that the large S abundance deduced from spectral fitting is real. The fitting statistics improve further when a nonthermal spectral energy component is included in the model (Table A.2 and Fig. A.2). Finally, the spectral models which include the K-shell edges were considered, but no meaningful constraints on the presence of the edges could be obtained.

Appendix B: X-ray properties of the nebula

The Extended Source Analysis Software package (ESAS) Snowden et al. (2004, 2008), which is integrated in the SAS, was employed to obtain the images and spectra of the diffuse emission. Following the data reductions steps prescribed by the *XMM-Newton* data analysis threads and the ESAS cookbook[4], the EPIC images were created in “soft” (0.2–0.7 keV), “medium” (0.7–1.2 keV), and “hard” (1.2–7.0 keV) energy bands. The background was modeled and subtracted, and the individual images were merged after correcting them by their corresponding exposure maps. Each image in each band was adaptively smoothed, requiring 50 counts under the smoothing kernel. The resultant exposure-corrected and background-subtracted color-composite image of the sky in the vicinity of IRAS 00500+6713 is shown in Fig. 1.

The background and the point-source corrected spectra of the nebula, as well as the corresponding response matrices, were extracted for each camera (MOS1, MOS2, pn) and for each observation (Fig. A.3) using the *pn-spectra*, *pn-back*, *mos-spectra*, and *mos-back* tasks in the ESAS package. All spectra were simultaneously fit with the abundances tied between different model temperature components. As recommended by the ESAS Cookbook, the spectra were fit in the 0.4–7.0 keV range. To account for the instrumental background produced by the fluorescence lines of Al Kα ($E \sim 1.49$ keV) and Si Kα ($E \sim 1.75$ keV) in the MOS cameras and the Al Kα line in the pn camera, we used the EPIC instrumental background files produced with the filter wheel equipped in the “CLOSED” position. For this reason, we employed the SAS task *evqpd* and produced a tailored “Filter Wheel Closed” (FWC) event file for both our observations. Spectra were extracted from the FWC files in the same area and at the same detector position as our science nebula spectra. The Al Kα and Si Kα lines were fit as Gaussians and thus their normalizations were determined. For the next step, these lines were added to the spectral model. As a result, the model *tbabs(vapec+vapec)+gauss(1.49 keV)* was used to fit pn spectra (Fig. A.3), while *tbabs(vapec+vapec)+gauss(1.49 keV)+gauss(1.75 keV)* was used for the MOS spectra (Fig. A.4).

Two temperature plasma models reproduce the spectra well when abundances are allowed to vary. These are the first ever spectra of the nebula in IRAS 00500+6713; therefore, there are no prior constraints on nebula abundances. From testing various models, the nitrogen abundance is not constrained and

[4] https://xmm-tools.cosmos.esa.int/external/sas/current/doc/esas/

Table B.1. X-ray spectral properties of the nebula in IRAS 00500+6713 from fitting its low-resolution EPIC pn (Fig. A.3) and MOS (Fig. A.4) spectra.

Model parameter	fit value		
N_H [10^{22} cm^{-2}]	1.1 ± 0.3	1.1 ± 0.3	1
kT_1 [keV]	0.11 ± 0.0	0.11 ± 0.01	0.13 ± 0.01
EM_1 [10^{54} cm^{-3}]	260 ± 90	41 ± 16	27 ± 6
kT_2 [keV]	0.8 ± 0.1	1.1 ± 0.2	1.60 ± 0.15
EM_2 [10^{54} cm^{-3}]	3.2 ± 0.7	0.9 ± 0.2	1.6 ± 0.1
C	100	600	600
O	9 ± 4	46 ± 21	46
Ne	37 ± 13	201 ± 70	330 ± 100
Mg	15 ± 5	69 ± 26	33 ± 19
reduced χ^2	1.0 (232 d.o.f.)	1.0 (232 d.o.f.)	1.0 (189 d.o.f.)
Model F_X [erg cm^{-2} s^{-1}]	$(1.8 \pm 0.1) \times 10^{-13}$		$(2.2 \pm 0.1) \times 10^{-13}$
Luminosity L_X [erg s^{-1}]		$(3.0 \pm 0.2) \times 10^{34}$	

Notes. The spectral model is a the two temperature collisional plasma corrected for the interstellar medium (ISM) absorption *tbabs*(*vapec*+*vapec*)). The Gaussian lines describing the Al Kα and Si Kα lines for the MOS and Al Kα for the pn cameras were explicitly added to the background (see text). First column: the model parameters from fitting pn spectra with a carbon abundance frozen to C = 100. Second column: the same as in the first column model, but with a carbon abundance frozen to C = 600. Third column: the same as in the second column model, but for EPIC MOS. The abundances which are not shown in the table were kept at their solar values. Observed flux and de-reddened luminosity are in the 0.2–12.0 keV band assuming d = 3.1 kpc.

consistent with the absence of nitrogen. The absolute values of O, Ne, and Mg depend on the initial guess for the C abundance (Table B.1); however, it is important to note that independent of the assumed C-abundance, the relative to oxygen abundances are similar. Strikingly, these ratios are different from those derived for the central star (Table A.2).

Appendix C: Abundances

The abundances determined from the fitting of spectral models to the observed X-ray spectra of the central star and the nebula can be used to compute the metal mass ratios and fractions. We assume that all abundant elements are detected in optical and X-ray spectra. These elements are C, O, Ne, Mg, Si, and S. Denoting the mass fraction of the i-element as X_i, and normalizing the total mass to unity gives $\sum_i X_i = 1$ or

$$X_j \sum_i \frac{X_i}{X_j} = 1. \quad (C.1)$$

The element mass ratios are related to the element number fractions as

$$\frac{X_i}{X_j} = \frac{n_i}{n_j} \cdot \frac{A_i}{A_j}, \quad (C.2)$$

where n_i is the abundance by number and A_i is the atomic mass of the element i.

The parameters of the X-ray spectral models *vapec* and *bvtapec*, which we used to fit the spectra with the *Xspec* software are the metal element abundances by number relative to their solar values Asplund et al. (2009). Therefore,

$$\frac{X_i}{X_j} = \frac{n_i^{Xspec}}{n_j^{Xspec}} \cdot \frac{n_i^{\odot}}{n_j^{\odot}} \cdot \frac{A_i}{A_j}, \quad (C.3)$$

then, using Eq. (C.1) and values given in Tables A.2 and B.1, one can derive the mass fractions X_i as given in Table 1.

From the analysis of the optical spectrum, $n_C = 0.25$ and $n_O = 0.74$, or $n_C/n_O = 0.3$. Using $n_i^{Xspec} = n_i/n_i^{\odot}$, and calculating input parameters for carbon and oxygen, $n_C^{Xspec} = n_C/n_C^{\odot} = 929.368$ and $n_O^{Xspec} = n_O/n_O^{\odot} = 1510.82$, hence as an input ratio in *Xspec* $n_C^{Xspec}/n_O^{Xspec} = 0.615$. Solving Eq. (C.1) gives $X_O = 0.6634$, and then $X_i = X_O \times \frac{X_i}{X_O}$.

To estimate the mass of hot gas in the nebula, we made a crude assumption that the nebula only consists of C, O, Ne, and Mg. Since X-ray emitting gas is hot, we assumed that these ions are fully ionized. Assuming a constant density ρ, the spherical nebula mass is $M = \rho V = n_{ion} \mu m_H V$, where $V \approx 10^{56}\,\mathrm{cm}^3$. The emission measure of the nebula is $EM = V \mu \beta n_{ion}^2$, where $\beta \approx 1/2$ is the number of electrons per atomic mass unit, and $\mu = \sum A_i n_i / \sum n_i \approx 13$ is the mean ion mass. The EM was observationally constrained, inserting values from Table B.1 $M = m_H \sqrt{V \cdot EM \cdot \mu/\beta} \sim 0.1\,M_{\odot}$.